View metadata, citation and similar papers at core.ac.uk
brought to you by CORE
provided by EPub Bayreuth

ZAAC
Zeitschrift für anorganische und allgemeine Chemie
DOI: 10.1002/zaac.202000077
ARTICLE

High Temperature Stable Maghemite Nanoparticles Sandwiched between Hectorite Nanosheets

Kevin Ament,[a,b] Daniel R. Wagner,[a,b] Frederieke E. Meij,[a,b] Friedrich E. Wagner,[c] and Josef Breu*[a,b]

Dedicated to Prof. Dr. Juri Grin on the Occasion of his 65th Birthday

Abstract. Maghemite (γ-Fe_2O_3) is a metastable iron oxide phase and usually undergoes fast phase transition to hematite at elevated temperatures (>350 °C). Maghemite nanoparticles were synthesized by the polyol method and then intercalated into a highly swollen (>100 nm separation) nematic phase of hectorite. A composite of maghemite nanoparticles sandwiched between nanosheets of synthetic hectorite was obtained. The confinement of the nanoparticles hampered Ostwald ripening up to 700 °C and consequently the phase transition to hematite is suppressed. Only above 700 °C γ-Fe_2O_3 nanoparticles started to grow and undergo phase transition to α-Fe_2O_3. The structure and the phase transition of the composite was evaluated using X-ray diffraction, TEM, SEM, physisorption, TGA/DSC, and Mößbauer spectroscopy.

Introduction

Due to high abundancy and low toxicity iron oxides are applied as pigments in cosmetics, as advanced (photo-)oxidation catalyst in waste water treatment and for diagnostics, drug delivery, sensoring or magneto optical devices.[1] Iron(III) oxide crystallizes in four well known polymorphs (α, β, γ, and ε-phase). More recently, a new fifth polymorph, ζ-phase, was discovered under high pressure conditions.[2] All of them exhibit significantly different structural, physical and chemical properties and might be of use for different biomedical, catalytic or magnetic applications.[3] Parameters that affect the phase transitions were extensively studied.[4] Spinel type γ-Fe_2O_3 ($Fd\bar{3}m$) is thermodynamically metastable at room temperature and bulk maghemite undergoes a rapid phase transition to corundum type α-Fe_2O_3 ($R3\bar{c}$) at temperatures around 350 °C. ε-Fe_2O_3 ($Pna2_1$) and β-Fe_2O_3 ($Ia\bar{3}$) are only observed as nanoparticles.[5]

Moreover, calorimetric and computational data suggest that the relative thermodynamic stability of the different iron oxide phases may also change on the nanoscale.[6] For instance, for nanoparticulate γ-Fe_2O_3 the phase transition to hematite has been shown to be suppressed until a certain threshold size is reached that is normally above 10–20 nm.[7] A common way to shift the phase transition to higher temperature is coating or embedding of the particles into a matrix.[8] For instance, when nanoparticulate γ-Fe_2O_3 is coated by an amorphous silica shell, particle growth is prevented and the phase transition is retarded up to 1000 °C.[9] A silica xerogel loaded with low amounts of γ-Fe_2O_3 nanoparticles (molar ratio Fe/Si of 0.013) retards the phase transition up to 900 °C. When the molar ratio is increased to 0.2, α-Fe_2O_3 is already observed at 500 °C.[10]

Synthetic fluorohectorite (NaHec, $[Na_{0.5}]^{inter}[Mg_{2.5}Li_{0.5}]^{oct}[Si_4]^{tet}O_{10}F_2$) is a 2D layered silicate with permanent negatively charged nanosheets balanced by Na^+ cations in the interlayer space. NaHec can be gently delaminated into individual silicate layers by thermodynamically allowed, repulsive osmotic swelling.[11] This most gentle way of delamination preserves the diameter of pristine NaHec platelets and yields nanosheets with a thickness of 1 nm and lateral dimensions of 20 µm.[12] Consequently, even in very dilute suspensions (<1 wt%) the separation is insufficient to allow for free rotation of the nanosheets and instead of isotropic suspensions rather a nematic liquid crystalline phase is obtained.[13] The strong electrostatic repulsion of the negatively charged nanosheets forces the nanosheets to adopt a cofacial arrangement even with nanosheet separations exceeding 100 nm.[14] This nematic phase allows for "intercalation" of nanoparticles carrying a positive surface potential between the nanosheets. By sandwiching nanoparticles in the confined space between two negatively charged nanosheets Ostwald ripening can by retarded and phase transition from γ-Fe_2O_3 to α-Fe_2O_3 can be suppressed up to 700 °C.

* Prof. Dr. J. Breu
E-Mail: josef.breu@uni-bayreuth.de
[a] Bavarian Polymer Institute
University of Bayreuth
Universitätsstraße 30
95447 Bayreuth, Germany
[b] Department of Chemistry
University of Bayreuth
Universitätsstraße 30
95447 Bayreuth, Germany
[c] Physics Department E15
Technical University of Munich
85747 Garching, Germany
Supporting information for this article is available on the WWW under **http://dx.doi.org/10.1002/zaac.202000077** or from the author.
© 2020 The Authors. Published by Wiley-VCH Verlag GmbH & Co. KGaA. · This is an open access article under the terms of the Creative Commons Attribution License, which permits use, distribution and reproduction in any medium, provided the original work is properly cited.

Results and Discussion

Composite Synthesis, Characterization, and Location of the Nanoparticles

For intercalation of nanoparticulate γ-Fe_2O_3 a positive surface charge is required. We applied a polyol method that allows for modification of the surface with phospocholine post synthesis yielding a positive surface charge.[15] Briefly, a mixture of $FeCl_2 \cdot 4H_2O$ and $FeCl_3 \cdot 6H_2O$ was dissolved in diethylene glycol and ramped by 2 $K \cdot min^{-1}$ to 220 °C. After refluxing for two hours the dispersion was allowed to cool to 90 °C and [calcium (phospocholine)] chloride tetrahydrate was added (1 mmol in 20 g diethylene glycol). After precipitation with acetone and decantation of diethylene glycol, the nanoparticles were redispersed in water.

According to transmission electron micrographs (TEM), the as prepared nanoparticles exhibited a size of 5.5 ± 1.1 nm (100 particles, Figure 1A and B). According to dynamic light scattering (DLS) the hydrodynamic diameter was determined to be 6.9 ± 1.3 nm (Figure 1C). This value is higher than the core size determined by TEM as the hydrodynamic diameter probed by DLS also includes the capping ligand and the solvation shell. At a pH of 7 the particles had a positive surface charge with a ζ-potential of +42 mV. The aqueous dispersion was stable for several weeks when stored at room temperature. The amount of phospocholine capping ligand was determined to be 5.5 wt% according to thermogravimetric analysis (TGA, Figure 1D).

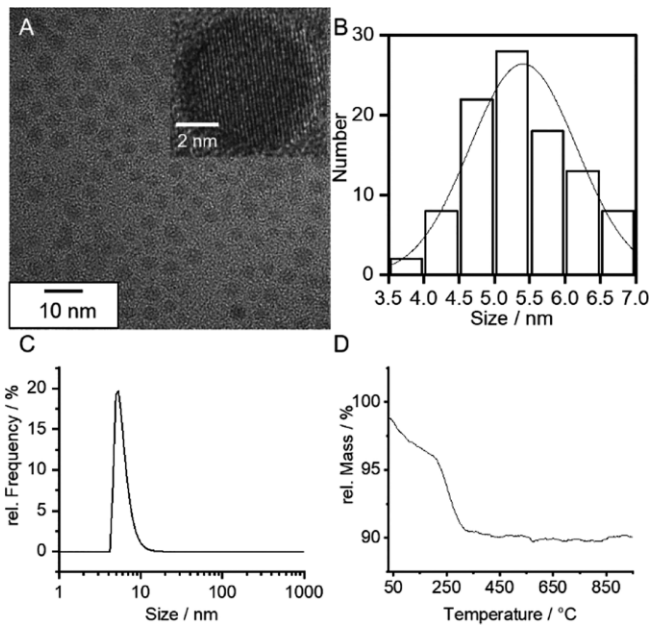

Figure 1. Analysis of nanoparticulate γ-Fe_2O_3 before intercalation. (A) TEM image of γ-Fe_2O_3 nanoparticles after synthesis. Inset: High magnification image. (B) Histogram of the core sizes of 100 particles. (C) Hydrodynamic diameter according to DLS measurement. (D) TGA measurement under flowing air.

NaHec powder was swollen in water to a nematic phase with a solid content of 1 wt%. This corresponded to a nanosheet separation of about 100 nm – much larger than the nanoparticle size of 5.5 nm. The aqueous NaHec dispersion was added rapidly to the aqueous nanoparticle dispersion under mechanical stirring with a weight ratio of γ-Fe_2O_3 and NaHec of 5:1. Upon addition hetero coagulation was triggered and after about one minute, visible flocculation occurred. The brown to orange flocculate was separated by a magnet from the still slightly brownish supernatant.

The loading level of γ-Fe_2O_3 was determined by inductively coupled plasma atomic absorption spectroscopy (ICP-AAS). The ratio of Fe to Si was determined to be 2.1:1. This corresponded to a nominal formula of $(Fe_2O_3)_{4.2}(Mg_{2.5}Li_{0.5}Si_4O_{10}F_2)$ or a weight fraction of 64 wt% γ-Fe_2O_3 (Table S1, Supporting Information).

The X-ray diffractogram (XRD) comprised two sets of reflections: In the low angle range a 00*l* (*l* = 1–3) series was observed corresponding to the one-dimensionally (1D) ordered intercalation compound (Figure 2A). The basal reflection (*001*) at 1.30° 2θ (6.9 nm) corresponds to the sum of silicate layer thickness (1 nm) and nanoparticle diameter (5.5 nm). The scanning electron microscopy (SEM) of the composite showed that upon flocculation with the nanoparticles the nanosheets restacked (Figure 2B).

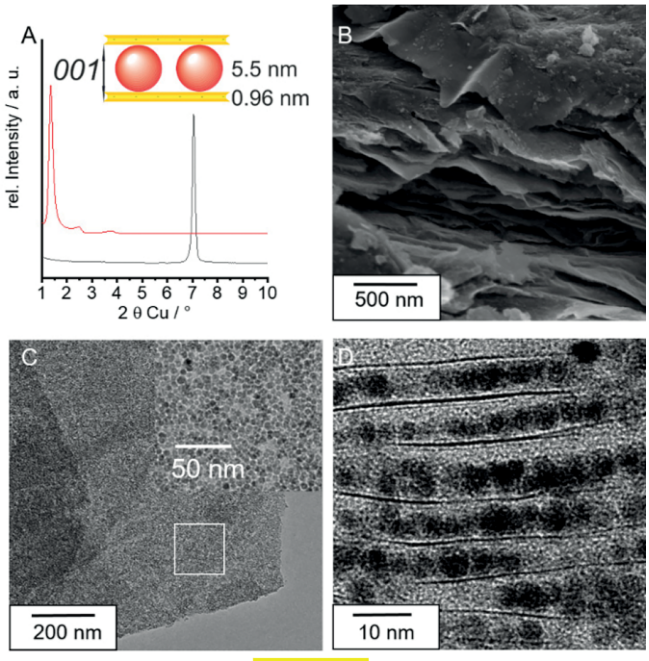

Figure 2. Structural analysis of the γ-Fe_2O_3/NaHec composite. (A) Red: XRD of textured sample of γ-Fe_2O_3/NaHec. Black: *001* of pristine NaHec for comparison. (B) SEM image of the restacked tactoid. (C) TEM image of top view of the composite. The inset shows the magnification of the white square of highly loaded nanosheets. (D) Cross sectional TEM image with view between the nanosheets.

TEM of the composite drop casted on a copper grid showed highly loaded platelets (Figure 2C). From these images it was not possible to identify the *z*-location of the particles nor could be distinguished between surface supported or intercalated. To overcome this problem, the composite was embedded in a resin and sliced applying an ultramicrotome. TEM images of this cross sections granted a look between the nanosheets. Well separated nanosheets with nanoparticles in between were ob-

© 2020 The Authors. Published by WILEY-VCH Verlag GmbH & Co. KGaA, Weinheim

served (Figure 2D). Due to the particle size distribution of γ-Fe_2O_3 the nanosheets could not restack perfectly parallel. The average periodicity as measured at 30 different sample spots gave a distance of 7.1 ± 1.2 nm, which is in decent agreement with the basal spacing observed in XRD. The varying distance of the nanosheets also is responsible for the broad reflections and the limited rationality of the *00l* series observed from the XRD (Figure 2A).

The second set of peaks in the XRD correspond to the intercalated nanoparticles and could be indexed with a cubic unit cell (space group $Fd\bar{3}m$) of a spinel type iron oxide phase (Figure 3A). No reflections of hematite or another crystalline iron oxide phase were observed. The reflections marked with circles are the *02*/*11* and the *06* bands of NaHec derived from the 2D crystal structure of the nanosheets in *ab* direction while the relative position along the *c* direction is random due to stacking faults.

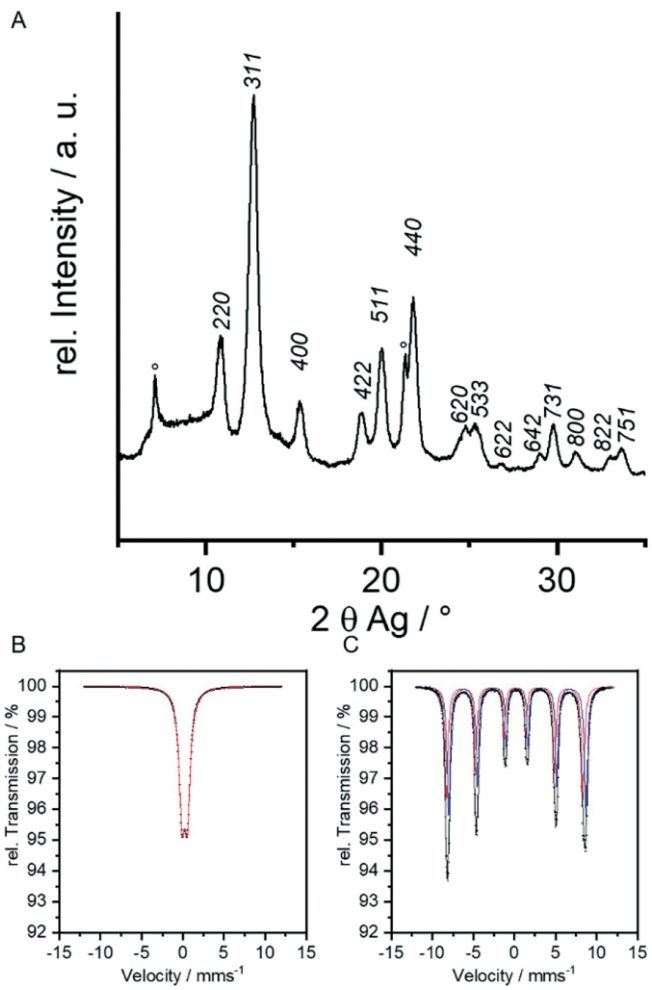

Figure 3. Evaluation of the phase of the γ-Fe_2O_3 nanoparticles in the composite. (A) Wide angle PXRD using Ag-K_α (λ = 0.5594075 Å) radiation. (B) Room temperature Mößbauer spectrum showing only one quadrupole doublet. (C) 4.2 K Mößbauer spectrum with two sextets for Fe^{3+} in tetrahedral sites (red) and octahedral sites (blue).

Since for the synthesis in air a mixture of Fe^{2+} and Fe^{3+} salts was applied to obtain a nanoscopic ferromagnetic phase, Mößbauer spectroscopy had to be employed to distinguish between the two spinel phases maghemite γ-Fe_2O_3 and magnetite Fe_3O_4. The RT spectrum showed only one quadrupole doublet due to fast superparamagnetic relaxation processes that is characteristic for small sized iron oxide nanoparticles (Figure 3B). The spectrum recorded at 4.2 K showed two sextets with nearly identical hyperfine fields and nearly no quadrupole interaction (Figure 3C). The isomeric shifts of 0.05 mm·s^{-1} and 0.33 mm·s^{-1} corresponded to the tetrahedral and octahedral sites of Fe^{3+}, respectively. Fe^{2+} that would indicate a magnetite phase could not be observed. Apparently, Fe^{2+} is readily oxidized to Fe^{3+} when exposed to air during synthesis. It should be noted that the direct synthesis of γ-Fe_2O_3 using single valent $FeCl_3$ always yielded microcrystalline hematite.

In the TEM micrograph, the γ-Fe_2O_3 nanoparticles appeared to be densely packed (Figure 2C and D). This, however, is an artefact caused by the superposition/projection of particles in the sample slice that is about 50 nm thick. The Ar-physisorption isotherm showed a type IV(a) behavior that corresponds to a mesoporous network (Figure S2A, Supporting Information). The shape of the hysteresis can be attributed to the H2(b) type. This type of hysteresis in the desorption branch normally is caused by a broad distribution of pore necks.[16] This is not surprising given the broad particles size distribution of γ-Fe_2O_3 acting as pillars. The surface area determined by BET method was 237 m^2·g^{-1} and the average pore size is 5.5 nm (Figure S2B). Clearly, the nanoparticles are not packed densely but rather a mesoporous material with open space between nanoparticles within a given interlayer space was obtained. This renders the composite also interesting for photocatalytic applications as short γ-Fe_2O_3 nanoparticles are stabiled on a substrate assuring short diffusion lengths of charge carriers.

Phase Transition

Deposition of nanoparticles on conventional (porous) supports as Al_2O_3 or SiO_2 normally allows only a very small loading. A higher loading triggers aggregation, blocking of pores of the support or fast Ostwald ripening. With the synthesis protocol presented here, the particle density was very high. One might consequently assume rather fast growth of the nanoparticles. The nanoparticles in the γ-Fe_2O_3/NaHec are, however, not conventionally supported on a single external surface, but were sandwiched between two negatively charged nanosheets.

To study the influence of confinement combined TGA and dynamic scanning calorimetry (DSC) in air was performed (Figure 4). An endothermic weight loss at the beginning can be attributed to desorption of interlayer water (ca. 5 wt%). The second weight loss of about 3.5 wt% can be attributed to the exothermic combustion of the phosphocholine capping ligand. Finally, a very broad exothermic event commenced at 800 °C without accompanying weight loss. This peak is related to the phase transition of γ-Fe_2O_3 to the thermodynamically more stable α-Fe_2O_3 phase.[4] The very broad peak suggests a rather sluggish transition.

© 2020 The Authors. Published by WILEY-VCH Verlag GmbH & Co. KGaA, Weinheim

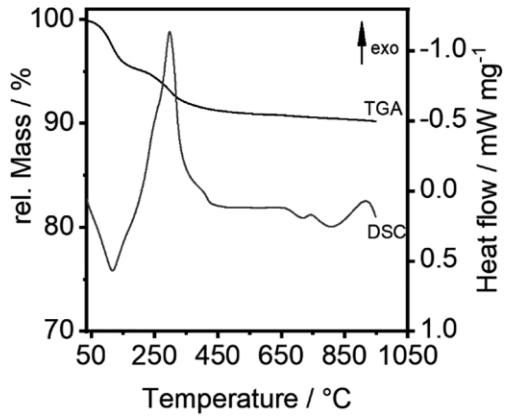

Figure 4. Thermal characterization of γ-Fe_2O_3/NaHec. TGA and DSC curves from 30 °C to 950 °C with a heating ramp of 10 K·min^{-1} and flowing air as atmosphere.

To rule out kinetic contributions to this high onset temperature of the phase transition, the composite was annealed at 700 °C for 20 h in air. No changes were observed in the PXRD pattern (Figure 5A), nor in the RT and 4.2 K Mößbauer spectra (Figure 5B and C). TEM analysis revealed that the nanoparticles retained their size within experimental error upon annealing (5.7 ± 1.2 nm, Figure 5F). Furthermore, the nanoparticles were still not faceted but spherical. The Ar-physisorption isotherm showed no significant changes upon annealing at 700 °C for 20 h (Figures S2C and S2D, Supporting Information, BET surface of 214 m^2·g^{-1} and an average pore size of 5.8 nm). All parameters thus indicated that the confinement between hectorite nanosheets retarded the growth of the particles. Moreover, as long as a certain threshold size is not exceeded, the phase transition to hematite was completely suppressed. It is noteworthy that Ostwald ripening and phase transition was retarded even at such high loadings and only by a sub nanometer thick "coating" layer. In contrast, when γ-Fe_2O_3 was coated by amorphous SiO_2 suppression of the phase transition required much thicker coatings.[9] Since γ-Fe_2O_3 that is precipitated on the external surface of the natural layered silicate montmorillonite[17] is only thermally stable up to 530 °C, the stabilization by the electrostatic attraction with only one negatively charged surface is insufficient. Apparently, the sandwich-like fixation from two directions is the crucial factor.

Please note that we apply a fluorohectorite that is far more stable than ordinary layered silicates containing hydroxyl groups. XRD, TEM, and TGA/DSC all gave no indication for the formation of a new solid phase.

Pushing it to the limit of thermal stability of NaHec for which decomposition starts at around 800 °C as evidenced by the decrease of intensity of the *02/11* band (Figure 5A), the phase transition can finally be triggered: When the composite is heated to 800 °C for 20 h, the PXRD exhibited a mixture of reflections of γ-Fe_2O_3 and α-Fe_2O_3. It was observed that the reflections of α-Fe_2O_3 were much sharper. This suggests that only the bigger particles that reached a certain size undergo phase transition. TEM images suggested (Figure 5G) that at this temperature intercalated γ-Fe_2O_3 nanoparticles gained

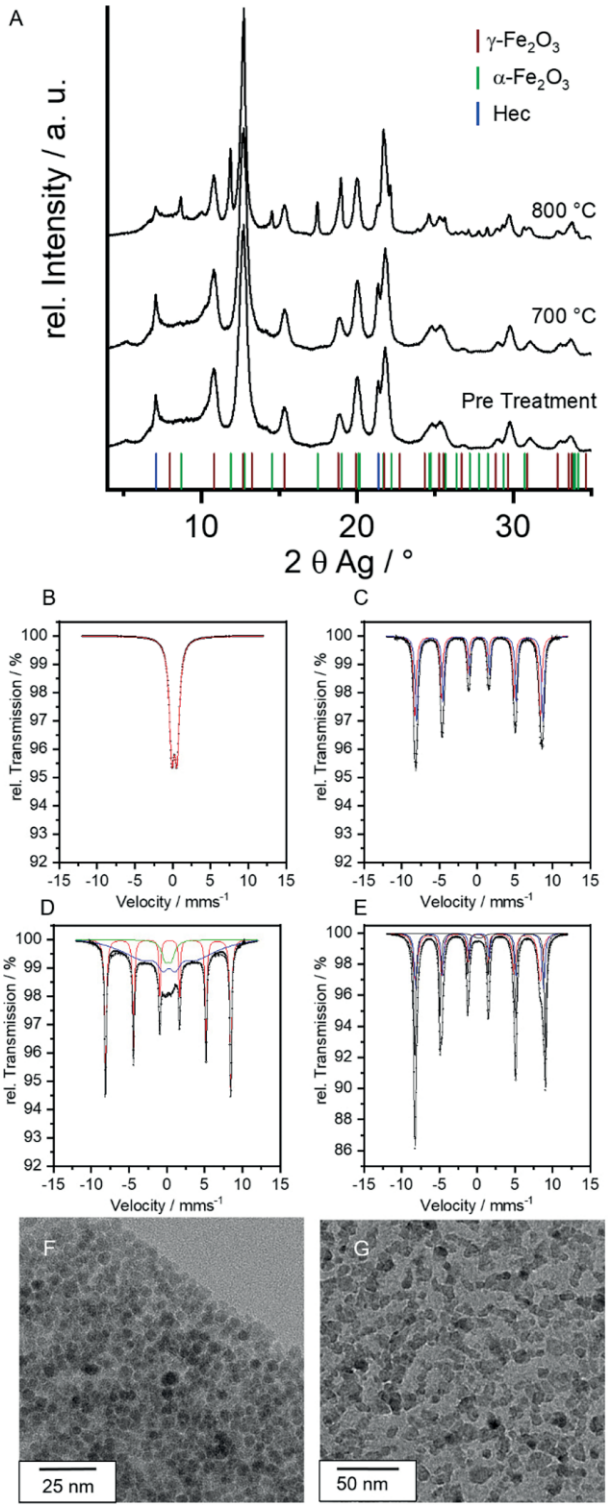

Figure 5. Evaluation of the phase and size of the γ-Fe_2O_3 nanoparticles in the composite after heat treatment. (A) Wide angle PXRD using Ag-K_α (λ = 0.5594075 Å) radiation. (B) + (C) Room temperature and 4.2 K Mößbauer spectra after treatment at 700 °C. (D) + (E) Room temperature and 4.2 K Mößbauer spectra after treatment at 800 °C. (F) + (G) TEM images after treatment at 700 and 800 °C.

enough mobility to be able to grow by coalescence to bigger nanoparticles (9.2 ± 2.3 nm). Furthermore, nanoparticles of irregular shape and dimensions of >20 nm were observed.

© 2020 The Authors. Published by WILEY-VCH Verlag GmbH & Co. KGaA, Weinheim

The 4.2 K Mößbauer (Figure 5E) spectrum showed not only the two sextets for the tetrahedral and octahedral sites of maghemite (hyperfine fields of 51.3 and 52.5 T, respectively), but an additional sextet (53.7 T) with a shift of 0.32 mm·s^{-1} which can be ascribed to well crystalline hematite particles capable of undergoing the Morin transition. According to area under the spectra the composition is 40 % hematite and 60 % maghemite. The RT spectrum (Figure 5D) exhibited a sextet originating from the hematite particles with an area of 41 %. The other very broad sextet belonged to maghemite particles with slower relaxation times as compared to the samples treated at 700 °C, which means that the particles were bigger in size. This is in accord with the bigger nanoparticles observed in the TEM image. The Ar-physisorption isotherm measured for the composite annealed at 800 °C was of type II, which corresponds to a nonporous or macroporous network and the BET surface was drastically reduced to 35 m^2·g^{-1} (Figure S2E, Supporting Information). This also was in line with a collapse of the porous structure upon annealing at 800 °C.

To stress the crucial role of the confinement by the hectorite nanosheets, dried unsupported nanoparticles were annealed as control (Figure S3, Supporting Information). Up to 400 °C the nanoparticles retained their size and phase as no changes in the PXRD were observed. After treatment at 450 °C microcrystalline hematite is the only phase observed. This indicated that also in agreement with results published by *Belin* et al.[7b] unsupported nanoparticles started ripening already above 400 °C accompanied by the phase transition. In contrast, the same nanoparticles confined between the hectorite nanosheets retained their size and phase at least up to 700 °C.

Conclusions

To hamper phase transition of nanoparticulate γ-Fe_2O_3 to α-Fe_2O_3 at higher temperature the size of the nanoparticles requires to be kept small.[4] The essential suppression of Ostwald ripening can be achieved by sandwiching γ-Fe_2O_3 nanoparticles between hectorite nanosheets. This can simply be achieved by "intercalation" of nanoparticles carrying a positive surface charge into highly swollen (>100 nm gallery height) nematic hectorite suspension. The electrostatic interaction with the negatively charged nanosheets retards Ostwald ripening of the nanoparticles up to 700 °C even at very high loadings (>60 wt%). As the nanoparticles retain their size, they consequently do not undergo phase transition to α-Fe_2O_3.

In general, wrapping with charged nanosheets of hectorite appears to represent an efficient tool to disperse and stabilize small nanoparticles. As the composite structures obtained are mesoporous, they should be interesting heterogeneous catalyst systems not only for Fe_2O_3, but for any kind of nanoparticles.[18] Since the accessible surface is preserved even to high temperatures, in particular catalytic reactions at high temperature[19] will be tested next.

Experimental Section

Materials: $FeCl_2$·$4H_2O$ (98 %), $FeCl_3$·$6H_2O$ (≥ 99 %), NaOH (pellets, ≥ 98 %) and diethylene glycol (99 %) were purchased from Sigma Aldrich. Phospchocholine chloride calcium salt tetrahydrate (98 %) was purchased from abcr GmbH. The water used was of MilliQ quality (18.2 MΩ). NaHec was synthesized via melt synthesis.[12]

Synthesis of γ-Fe_2O_3 Nanoparticles: Nanoparticles were obtained by a slightly modified published procedure.[15] $FeCl_2$·$4H_2O$ (398 mg, 1.00 mmol) and $FeCl_3$·$6H_2O$ (1,05 g, 2.00 mmol) were dissolved in 40.0 g diethylene glycol (DEG). NaOH (640 mg, 16.0 mmol) in 80.0 g DEG was added and the solution was degassed under a flow of argon for 3 h. The solution was heated to 220 °C with a ramp of 2 K·min^{-1} and kept at this temperature for 2 h. The dispersion was allowed to cool to 90 °C and phospchocholine chloride calcium salt tetrahydrate (330 mg, 1.00 mmol) in 20.0 g DEG was rapidly added under vigorous stirring. The temperature was kept for 1 h and then cooled to room temperature. The particles were precipitated in 600 mL of acetone, washed two times with 400 mL of acetone and then redispersed in water. The dispersion was dialyzed in 4 L of water for 48 h with water being exchanged after 6 and 24 h.

Synthesis of γ-Fe_2O_3/NaHec: NaHec was delaminated as 1 wt% dispersion in water. For the intercalation the pH of both NaHec and nanoparticle dispersions was adjusted to pH 7. NaHec was rapidly added to excess of particle dispersion under mechanical stirring. The flocculate was recovered by a magnet, washed 3 times and then dried at 80 °C. To remove organics adsorbed to the surface, the powder was calcined under a flow of clean air at 500 °C for 5 h.

Characterization: Hydrodynamic diameter and ζ-potential were recorded on a Litesizer 500 (Anton-Paar). Thermogravimetric analysis (TGA) and differential scanning calorimetry (DSC) were acquired with a Netzsch STA 449 F3 Jupiter with a heating ramp of 10 K·min^{-1} in flowing air. Textured X-ray diffraction patterns (XRD) at low angles were acquired on a Bragg–Brentano type diffractometer (Empyrean, PANalytical) with nickel filter and Cu-K_α radiation (λ = 1.54187 Å). The higher angle XRD patterns were recorded applying a STOE STADI-P equipped with four MYTHEN2 R 1 K detectors and Ag-K_α (λ = 0.5594075 Å). The samples were filled into 0.5 mm glass capillaries for this purpose. To determine the elemental composition to about 20 mg of the sample was added a mixture of 1.5 mL 30 wt% HCl (Merck), 0.5 mL of 85 wt% H_3PO_4 (Merck), 0.5 mL 65 wt% HNO_3 (Merck) and 1 mL of 48 wt% HBF_4 (Merck). The sample was digested in a MLS 1200 Mega microwave digestion apparatus for 6.5 min and heated at 600W (MLS GmbH). The sample was allowed to cool to room temperature and the clear solution was diluted to 100 mL and analyzed with a Varian AA100. Scanning electron microscopy (SEM) was performed on a Zeiss Ultra plus with an accelerating voltage of 3 kV. Transmission electron microscopy (TEM) images were acquired using a JEOL JEM-2200FS (200 kV). For cross sectional TEM the powder was embedded and was cut with a Leica Ultramicrotom UC7+FC7. Physisorption isothermes were recorded on a Quantachrome Autosorb-1 with argon as adsorbate at 87 K. The isotherms were evaluated using the Brunauer-Emmet-Teller (BET) method and the pore size distribution was calculated with the NLDFT method. The Mößbauer measurements were performed in transmission geometry with a spectrometer operating with a sinusoidal velocity waveform. The source was about 25 mCi of ^{57}Co in rhodium. The gamma rays were detected with a proportional counter filled with a krypton/CO_2 mixture. Measurements at liquid helium temperature were performed in a liquid helium bath cryostat, in which both the source and the absorber were cooled to 4.2 K.

Supporting Information (see footnote on the first page of this article): Results of ICP-AAS, Ar-physisorption and control study of unsupported nanoparticles.

© 2020 The Authors. Published by WILEY-VCH Verlag GmbH & Co. KGaA, Weinheim

Acknowledgements

This work was supported by the Deutsche Forschungsgemeinschaft (SFB 840). We thank *Marco Schwarzmann* for preparing TEM samples and *Lena Geiling* for performing SEM. We thank *Stefan Rettinger* for TGA/DSC measurements. We appreciate the support of the Keylab for Optical and Electron Microscopy of the Bavarian Polymer Institute (BPI). KA thanks the Elite Network of Bavaria (ENB) for a research fellowship and the elite study program "Macromolecular Science" for a fellowship. Open access funding enabled and organized by Projekt DEAL.

Keywords: Hectorite; Layered compounds; Iron oxide; Phase transitions; Temperature stability

References

[1] a) M. Sugimoto, *J. Am. Ceram. Soc.* **1999**, *82*, 269–280; b) Z. Tianshu, L. Hongmei, Z. Huanxing, Z. Ruifang, S. Yusheng, *Sens. Actuators B* **1996**, *32*, 181–184; c) W. Shangguan, A. Yoshida, *J. Phys. Chem. B* **2002**, *106*, 12227–12230; d) L. Han, S. Cai, M. Gao, J. Y. Hasegawa, P. Wang, J. Zhang, L. Shi, D. Zhang, *Chem. Rev.* **2019**, *119*, 10916–10976; e) Y. Shi, H. Li, L. Wang, W. Shen, H. Chen, *ACS Appl. Mater. Interfaces* **2012**, *4*, 4800–4806; f) M. M. Fernandes, H. Mora, E. D. Barriga-Castro, C. Luna, R. Mendoza-Reséndez, C. Ribeiro, S. Lanceros-Mendez, P. Martins, *J. Phys. Chem. C* **2018**, *122*, 19189–19196.

[2] J. Tuček, L. Machala, S. Ono, A. Namai, M. Yoshikiyo, K. Imoto, H. Tokoro, S. Ohkoshi, R. Zbořil, *Sci. Rep.* **2015**, *52*, 15091.

[3] a) A. Kay, I. Cesar, M. Grätzel, *J. Am. Chem. Soc.* **2006**, *128*, 15714–15721; b) G. Carraro, D. Barreca, M. Cruz-Yusta, A. Gasparotto, C. Maccato, J. Morales, C. Sada, L. Sánchez, *ChemPhysChem* **2012**, *13*, 3798–3801; c) Y. Zhu, L. P. Stubbs, F. Ho, R. Liu, C. P. Ship, J. A. Maguire, N. S. Hosmane, *ChemCatChem.* **2010**, *2*, 365–374.

[4] L. Machala, J. Tuček, R. Zbořil, *Chem. Mater.* **2011**, *23*, 3255–3272.

[5] S. Sakurai, A. Namai, K. Hashimoto, S. Ohkoshi, *J. Am. Chem. Soc.* **2009**, *131*, 18299–18303.

[6] a) A. Navrotsky, C. Ma, K. Lilova, N. Birkner, *Science* **2010**, *330*, 199; b) A. Navrotsky, L. Mazeina, J. Majzlan, *Science* **2008**, *319*, 1635.

[7] a) F. S. Yen, W. C. Chen, J. M. Yang, C. T. Hong, *Nano Lett.* **2002**, *2*, 245–252; b) T. Belin, N. Millot, N. Bovet, M. Gailhanou, *J. Solid State Chem.* **2007**, *180*, 2377–2385; c) S. Lee, H. Xu, *J. Phys. Chem. C* **2016**, *120*, 13316–13322.

[8] R. Zboril, A. Bakandritsos, M. Mashlan, V. Tzitzios, P. Dallas, C. Trapalis, D. Petridis, *Nanotechnology* **2008**, *19*, 095602.

[9] E. Taboada, M. Gich, A. Roig, *ACS Nano* **2009**, *3*, 3377–3382.

[10] P. P. C. Sartoratto, K. L. Caiado, R. C. Pedroza, S. W. da Silva, P. C. Morais, *J. Alloys Compd.* **2007**, *434–435*, 650–654.

[11] a) A. Lerf, *Dalton Trans.* **2014**, *43*, 10276–10291; b) M. Daab, N. J. Eichstaedt, A. Edenharter, S. Rosenfeldt, J. Breu, *RSC Adv.* **2018**, *8*, 28797–28803; c) M. Daab, N. J. Eichstaedt, C. Habel, S. Rosenfeldt, H. Kalo, H. Schiessling, S. Forster, J. Breu, *Langmuir* **2018**, *34*, 8215–8222.

[12] M. Stöter, D. A. Kunz, M. Schmidt, D. Hirsemann, H. Kalo, B. Putz, J. Senker, J. Breu, *Langmuir* **2013**, *29*, 1280–1285.

[13] S. Rosenfeldt, M. Stöter, M. Schlenk, T. Martin, R. Q. Albuquerque, S. Förster, J. Breu, *Langmuir* **2016**, *32*, 10582–10588.

[14] Z. Wang, K. Rolle, T. Schilling, P. Hummel, A. Philipp, B. A. F. Kopera, A. M. Lechner, M. Retsch, J. Breu, G. Fytas, *Angew. Chem.* **2020**, *132*, 1302–1310.

[15] a) H. Qu, D. Caruntu, H. Liu, C. J. O'Connor, *Langmuir* **2011**, *27*, 2271–2278; b) K. Araki, M. Uchiyama, S. Toma, S. Rodrigues, A. Shimada, R. Loiola, H. Rodriguez, P. Oliveira, M. Luz, S. Rabbani, H. Toma, S. H. P. Farsky, *Int. J. Nanomed.* **2015**, 4731–4731.

[16] M. Thommes, K. Kaneko, A. V. Neimark, J. P. Olivier, F. Rodriguez-Reinoso, J. Rouquerol, K. S. W. Sing, *Pure Appl. Chem.* **2015**, *87*, 1051–1069.

[17] Z. Orolínová, A. Mockovčiaková, V. Zeleňák, M. Myndyk, *J. Alloys Compd.* **2012**, *511*, 63–69.

[18] J. Hühn, C. Carrillo-Carrion, M. G. Soliman, C. Pfeiffer, D. Valdeperez, A. Masood, I. Chakraborty, L. Zhu, M. Gallego, Z. Yue, M. Carril, N. Feliu, A. Escudero, A. M. Alkilany, B. Pelaz, P. del Pino, W. J. Parak, *Chem. Mater.* **2016**, *29*, 399–461.

[19] A.-H. Lu, J.-J. Nitz, M. Comotti, C. Weidenthaler, K. Schlichte, L. C. W. O. Terasaki, F. Schüth, *J. Am. Chem. Soc.* **2010**, *132*, 14152–14162.

Received: February 17, 2020
Published Online: April 1, 2020

 © 2020 The Authors. Published by WILEY-VCH Verlag GmbH & Co. KGaA, Weinheim